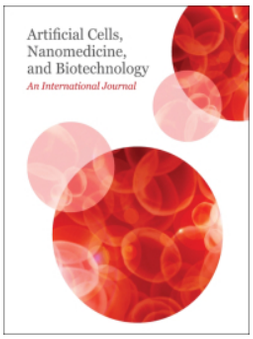

Taylor & Francis
Taylor & Francis Group

Artificial Cells, Nanomedicine, and Biotechnology
An International Journal

ISSN: (Print) (Online) Journal homepage: www.tandfonline.com/journals/ianb20

Panicum maximum Jacq. mediated green synthesis of silver nanoparticles: synthesis, characterization, and biological activities supported by molecular docking

Heba W. Alhamdi, Hanan Khalaf Anazi, Fatma Alzahraa Mokhtar, Seham S. Elhawary, Serag Eldin I. Elbehairi, Mohammad Y. Alfaifi, Ali A. Shati, Lamiaa I. Fahmy, Engy Elekhnawy, Afnan Hassan, Walaa A. Negm, Sherif Ashraf Fahmy & Nabil Selim

To cite this article: Heba W. Alhamdi, Hanan Khalaf Anazi, Fatma Alzahraa Mokhtar, Seham S. Elhawary, Serag Eldin I. Elbehairi, Mohammad Y. Alfaifi, Ali A. Shati, Lamiaa I. Fahmy, Engy Elekhnawy, Afnan Hassan, Walaa A. Negm, Sherif Ashraf Fahmy & Nabil Selim (2024) *Panicum maximum* Jacq. mediated green synthesis of silver nanoparticles: synthesis, characterization, and biological activities supported by molecular docking, Artificial Cells, Nanomedicine, and Biotechnology, 52:1, 411-425, DOI: 10.1080/21691401.2024.2395811

To link to this article: https://doi.org/10.1080/21691401.2024.2395811

Published online: 28 Aug 2024.

ARTIFICIAL CELLS, NANOMEDICINE, AND BIOTECHNOLOGY
2024, VOL. 52, NO. 1, 411–425
https://doi.org/10.1080/21691401.2024.2395811

Panicum maximum Jacq. mediated green synthesis of silver nanoparticles: synthesis, characterization, and biological activities supported by molecular docking

Heba W. Alhamdi[a], Hanan Khalaf Anazi[b], Fatma Alzahraa Mokhtar[c,d], Seham S. Elhawary[e], Serag Eldin I. Elbehairi[f,g], Mohammad Y. Alfaifi[f,g], Ali A. Shati[f,g], Lamiaa I. Fahmy[h], Engy Elekhnawy[i], Afnan Hassan[j], Walaa A. Negm[k], Sherif Ashraf Fahmy[l] and Nabil Selim[e]

[a]Department of Biology, College of Sciences, King Khalid University, Abha 61413, Saudi Arabia; [b]Department of Biology, Collage of Science, Tabuk University, Tabuk, Saudi Arabia; [c]Fujairah Research Centre, Sakamkam Road, Fujairah, United Arab Emirates; [d]Department of Pharmacognosy, Faculty of Pharmacy, El Saleheya El Gadida University, El Saleheya El Gadida 44813, Sharkia, Egypt; [e]Pharmacognosy Department, Faculty of Pharmacy, Cairo University, Kasr-El-Ainy Street, Cairo 11562, Egypt; [f]Tissue Culture and Cancer Biology Research Laboratory, King Khalid University, Abha, 9004, Saudi Arabia; [g]King Khalid University, Faculty of Science, Biology Department, Abha 9004, Saudi Arabia; [h]Department of microbiology and immunology, Faculty of Pharmacy, October University for Modern Sciences and Arts (MSA), Giza, Egypt; [i]Department of Pharmaceutical Microbiology, Faculty of Pharmacy, Tanta University, Tanta 31527, Egypt; [j]Biomedical Sciences Program, University of Science and Technology, Zewail City of Science and Technology, Cairo, 12578, Egypt; [k]Department of Pharmacognosy, Faculty of Pharmacy, Tanta University, Tanta 31527, Egypt; [l]Department of Chemistry, School of Life and Medical Sciences, University of Hertfordshire Hosted by Global Academic Foundation, R5 New Garden City, New Capital, Cairo 11835, Egypt

ABSTRACT

This study uses the aerial parts of *Panicum maximum* total extract (PMTE) to synthesize silver nanoparticles (AgNPs) in an environmentally friendly manner. TEM, SEM, FTIR, X-ray powder diffraction (XRD), Zeta potential, UV, and FTIR were used to characterize the green silver nanoparticles (PM-AgNPs). PM-AgNPs were evaluated as anticancer agents compared to (PMTE) against breast (MCF-7), lung (A549), and ovary adenocarcinoma (SKOV3) human tumour cells. The antibacterial activity of AgNPs was assessed against *Staphylococcus aureus* isolates. The PM-AgNPs had an absorbance of 418 nm, particle size of 15.18 nm, and zeta potential of −22.4 mV, ensuring the nanosilver's stability. XRD evaluated the crystallography nature of the formed PM-AgNPs. The cytotoxic properties of PM-AgNPs on MCF-7 and SKOV 3 were the strongest, with IC50s of 0.13 ± 0.015 and 3.5 ± 0.5 g/ml, respectively, as compared to A549 (13 ± 3.2 µg/mL). The increase in the apoptotic cells was 97.79 ± 1.61 and 96.6 ± 1.91% for MCF-7 and SKOV3 cell lines, respectively. PM-AgNPs were found to affect the membrane integrity and membrane permeability of 50 and 43.75% of the tested isolates, respectively. Also, PM-AgNPs have recorded a reduction in the biofilm formation of *S. aurues*. These results suggest using PM-AgNPs to treat breast and ovarian cancers.

GRAPHICAL ABSTRACT

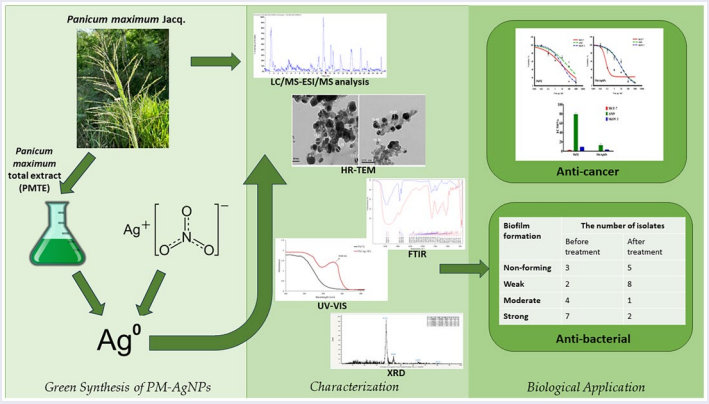

ARTICLE HISTORY

Received 15 April 2024
Revised 28 May 2024
Accepted 12 July 2024

KEYWORDS

Green synthesis; silver nanoparticles; anticancer; antibiofilm; apoptosis

CONTACT Fatma Alzahraa Mokhtar fatma.mohammed@frc.ae Fujairah Research Centre, Fujairah, United Arab Emirates; Sherif Ashraf Fahmy sheriffahmy@aucegypt.edu Department of Chemistry, School of Life and Medical Sciences, University of Hertfordshire Hosted by Global Academic Foundation, R5 New Garden City, New Capital, Cairo 11835, Egypt

Introduction

Panicum maximum is a small, creeping rhizome comprising perennial, tufted grass. This robust grass has stems that can grow up to 2 m tall. At the base of the stem, leaf sheaths are covered with tiny hairs that serve as protection. *Panicum maximum* keeps its green hue far into the cold months. The leaves can be up to 35 mm wide and have sharp edges. They then narrow down to a long, thin point. A big multiple-fanned inflorescence with an open panicle, free-hanging branches, and flexuous leaves is present. Usually, the lower floret is male and has a higher bract that covers the flower and a well-developed palea [1,2]. *Panicum maximum* is a natural forage plant of significant commercial importance in Africa, and it was imported as a source of animal feed in practically all tropical nations. It was originally served in North Africa's dry regions (Morocco, Libya, Algeria, Tunisia, and Egypt) [2,3]. Several studies reported the powerful antioxidant properties of *Panicum maximum,* making it a perfect candidate for the green synthesis of metallic nanoparticles *via* acting as natural reductant and capping agent [2,3]. Nanotechnology has impacted and advanced numerous scientific fields and led to the fabrication of various smart nanoparticles with improved biomedical applications. Silver nanoparticles (AgNPs), among others, have drawn much attention to their distinctive characteristics [4,5]. Feynman first mentioned nanotechnology in 1959. Thanks to nanotechnology, a wide range of industries have nourished, especially pharmaceuticals and health care [6,7].

Given the variety of readily available plants and their simple and secure application, plant-mediated synthesis of AgNPs is a widely employed strategy. Many plant parts, such as leaves, extracts, fruits, and flowers have been successfully employed in nanoparticles green synthesis. Plant extracts contain a wide range of bioactive compounds, such as vitamins, enzymes, proteins, amino acids, terpenoids, tannins, saccharides, phenols, and flavonoids. These functional biomolecules are present in plant extracts, making it easier and more stable to synthesize bioactive AgNPs employing plants [6–8].

Owing to the high rate of resistance development that emerges from pathogenic bacteria, it is important to reveal novel agents that have antibacterial potential [9]. In the current investigation, AgNPs were elucidated for their antibacterial potential towards *Staphylococcus aureus* isolates. *S. aureus* is a typical normal flora in the human body, and it is capable of causing a wide range of skin infections and its high resistance and mutation rates have developed life-threatening new strains [10]. In addition, it has many virulence factors that complicate its treatment, such as the ability to produce various enzymes and toxins and the ability to form biofilm [11]. So, it is essential to elucidate alternative approaches for treating ailments caused by these pathogenic bacteria. This study aims to evaluate the phytochemical profiling of *Panicum maximum* and its biological activities, including antimicrobial, antioxidant, and cytotoxic activities. To the best of our knowledge, we are the first to study the nanoformulation of AgNPs using the phytoconstituents of the green aerial parts of *Panicum maximum* that served as bioreductant and capping agent. The synthesized AgNPs exhibited potent antioxidant, anticancer and antoimicrobial activities.

Materials and methods

Plant extract preparation

The green aerial parts of *Panicum maximum* Jacq. were collected from the Alkeram farms in Wadi Alnatreoon, Egypt. A private farm owned by one of the authors (Dr. Fatma Alzahraa Mokhtar) so no permission was needed. The plant specimens were identified by Dr Esra Amaar, a plant scientist at Tanta University. The voucher specimens (PG-A-PM-F-18) were established at Tanta University's Herbarium. One kilogram of the plant was dried and ground into powder. The extract was prepared using the hot decoction method three successive times, each for 1 h. The extract was filtered thoroughly by filter paper and lyophilized. The resulting powder extract was kept for LC/MS-ESI/MS analysis, nanoparticle synthesis, and biological evaluation.

LC/MS-ESI/MS analysis

The *Panicum maximum* aerial parts chemical identification was analyzed by implementing the methods previously described by Albalawi et al. [12]. Briefly, HSS T3 columns (Waters Corporation, Milford, MA, USA) were utilized for chromatographic separation. A 0.5 m × 3.0 mm precolumn (Phenomenex, Torrance, CA, USA). Columns were kept at 40 °C. Mobile phase (A) pH was adjusted to 8 with sodium hydroxide. The mobile phase was 1% methanol with 5 mM ammonium formate. A binary gradient elution system was applied. The experiment employed IDA (information-dependent acquisition). MS and MS/MS data collection batches were prepared using Analyst-TF 1.7.1. IDA simplified full-scan MS and MS/MS data capture. The high-resolution survey spectra covered the mass-to-energy range of 50–1000 m/z.

Green synthesis of PM-AgNPs

One gram of plant extract was dissolved in 50 distilled H_2O, and an aliquot of 10 ml was added to a 90 ml 1Mm $AgNO_3$ solution in the dark. Observing the reaction every 30 min, it was completed after 5 h in comparison to a standard solution of 1 mM $AgNO_3$. Upon reaction completion, the nanoparticle solution was centrifuged for 30 min at 3000 rpm, then washed thoroughly three times with distilled H_2O, followed by washing three times with 100% ethanol for further purification.

Characterization of PM-AgNPs

Physical inspection

Reactions were completed upon observing the opaque appearance in the reaction container and a dark precipitate formation.

Ultraviolet-visible (UV-vis) spectroscopy

Using a spectrophotometer (Shimadzu, Kyoto, Japan), the wavelength of maximum absorbance was examined through UV-Vis spectra in the 300–800 nm range [13–15].

Infra-red spectroscopy

Fourier-transform infra-red spectroscopy (FTIR) in attenuated total reflectance (ATR) mode on a PerkinElmer System 2000 analyzer was used to examine and ascertain the adsorption of functional groups of both the plant extract and the greenly produced AgNPs. The KBr pelland et method was employed. The pellets that were of poor quality were not included for accurate measurements. The transmittance values were averaged and plotted against wavelength following the three recordings of each sample's spectra. To identify the functional groups, the FT-IR spectrum was studied and compared to the absorption band values of 14 [16,17].

Morphological features using transmission electron microscopy

HR-TEM (JEOL-JEM-2100, Kyoto, Japan) operating at 200 kV and TEM (JEOL-JEM-1011, Kyoto, Japan) were used for studying the morphology of the greenly synthesized AgNPs.

Zeta potential

At 25 °C, sample's zeta potential was evaluated using a Zeta Sizer Nano ZN (Malvern Panalytical Ltd., England, UK). Values were measured at a final concentration of 100 µg/ml, with continuous pH measurements made before each measurement [18].

X-ray diffraction (XRD)

XRD analysis was used to evaluate and validate the surface chemical analysis of the formed nanoparticles, including their phase and crystallinity. The analysis was conducted at room temperature using an XPERT-PRO-PANalytical Powder Diffractometer (PANalytical B.V., Almelo, The Netherlands) and a monochromatic radiation source Cu-Kα radiation at 45 kV and 30 mA, "where Cu-Kα radiation ($\theta = 1.5406$ Å)". Data on PM-AgNPs intensity were collected within a 2θ range of 4.01–79.99°.

Antioxidant activity of PMTE

ABTS radical scavenging capacity

The procedure was followed to scavenge free radicals using ABTS [19]. 10 ml of ABTS (7 mM in H_2O) and 10 ml of potassium persulfate (2.45 mM in H_2O) were combined to create the working ABTS + solution, which was then further incubated for 12 h in the dark. Subsequently, water was added to the ABTS + solution to achieve an absorbance of 0.700 ± 0.03 at 405 nm. Subsequently, 190 µl of ABTS + solution was combined with 10 µl of extracts (1, 0.1, or 0.01 mg/ml) and incubated for 30 min. At 405 nm, the absorbance was measured following incubation. Trolox was utilized as a control.

Ferric-ion-reducing antioxidant power (FRAP) assay

The earlier procedure [20] was followed in conducting the FRAP ability assay of PM extract. In summary, 15 ml of acetate buffer, 1.5 ml of TPTZ solution, and 1.5 ml of $FeCl_3$—$6H_2O$ were combined with 10 µl of extracts (final concentration in well: 0.34, 0.034, and 0.0034 mg/ml) in 290 µl of a working solution. For 30 min, the mixture was incubated. The absorbance was then calculated at 593 nm. We used Trolox as a control [21].

In vitro cytotoxic activity of PMTE

Cytotoxicity assay and cell cycle analysis

Human cell lines for breast (MCF-7), lung (A549), and ovarian (SKOV3) cancers were acquired from the American Type Culture Collection (ATCC). The cytoxicity of PMTE and PM-AgNPs was assessed against the three cancer cell lines utilizing the Sulphorhodamine B test (SRB). For cell cycle analysis The chosen cancer cell lines were treated with PMTE and PM-AgNPs for 48 h after the IC_{50} values for each were predetermined. Treatment was followed by trypsinization and two times of phosphate buffered saline (PBS) washing. Treated cells were resuspended in 500 µL of RNase staining buffer containing propidium iodide (PI) followed by incubation for a duration of 15 min. Finally, the data from 10,000 cells were evaluated using FACS analysis utilizing a Cytek® Northern Lights 2000 spectral flow cytometer (Cytek Biosciences) and SpectroFlo™ Software version 2.2.0.3 (Cytek Biosciences) to determine cell cycle phases distribution [22].

Apoptosis analysis

Following a 48 h treatment with PMTE and PM-AgNPs, MCF-7, A549, and SKOV3, trypsinization and PBS washing, apoptosis was assessed using the Annexin V-FITC/PI Apoptosis Detection Kit. The cells were reconstituted in five microliters of Annexin V-FITC, followed by five microliters of PI (staining solution) and 0.5 ml of binding buffer. The mixture was gently mixed and left under dark conditions at room temperature for 15 min. Lastly, SpectroFlo™ Software version 2.2.0.3 (Cytek Biosciences), USA, was used to apply the cells to FACS analysis utilizing a Cytek® Northern Lights 2000 spectral flow cytometer (Cytek Biosciences) [23].

Antibacterial activity

Agar well diffusion and determination of minimum inhibitory concentration (MIC)

The antibacterial potential of PM-AgNPs was determined against sixteen *S. aureus* bacteria by means of the agar well diffusion technique. Next, on 96-well microtitration plates, the MIC values were determined by employing the broth microdilution technique [24]. The lowest dose, or MIC, completely suppresses bacterial growth.

Impact on the membrane integrity and permeability

By monitoring the material discharge with absorption at 260 nm, as previously described [25,26], the effect of PM-AgNPs on bacterial membrane integrity was examined. The bacterial isolates' optical density (OD) was adjusted to 0.4 and the obtained pellet, upon centrifugation, was resuspended in saline solution for UV-Vis spectrophotometer (SHIMADZU, Japan) measurement at 260 nm. O-nitropheny

l-β-galactopyranoside (ONPG), which is converted by the enzyme into *O*-nitrophenol (ONP), was used to record the release of β-galactosidase enzyme from the bacterial cells to determine the membrane permeability. Then, using an ELISA reader (Sunrise Tecan, Austria), the absorbance at 420 nm was used to quantify ONP [27,28].

Impact on biofilm formation by crystal violet assay

The crystal violet experiment demonstrated the tested isolates' ability to produce biofilms [29,30]. The tested isolates were categorized as previously described [8,31] into non-biofilm, mild, moderate, and strong biofilm-forming isolates using OD values measured at 490 nm in 96-well microtitration plates.

In silico study

Molecular docking

PM extract was found to exert its anticancer activity on breast and ovarian cancer cell lines. Two crystal structures were chosen: oestrogen receptor alpha represents the breast tumour cell line (MCF-7), and the second is poly (ADP-ribose) polymerase (PARP) for the ovary adenocarcinoma human tumour cell line (SKOV3). The two Crystal structures were retrieved from the Protein Data Bank; human oestrogen receptor alpha (ERα) in complex with 4-hydroxy tamoxifen (PDB ID: 3ERT) with a resolution of 1.90 Å, R-Value Work of 0.262, and R-Value Free of 0.229 and the second one is poly(ADP-ribose) polymerase (PARP) in complex with 2-[4-[(2S,3S,4R,5R)-5-(6-aminopurin-9-yl)-3,4-bis (oxidanyl) oxolan-2-yl] carbonyl piperazin-1-yl]-N-(1-oxidanylidene-2,3-dihydroisoindol-4-yl) ethanamide (PDB ID: 5DSY) with resolution of 2.70 Å, R-value work of 0.193, and R-value free of 0.248) [32,33]. The two receptor structures were prepared using AutoDock4, and all water molecules and ligands were eliminated. Using the ADT's prepare_receptor4.py command, polar hydrogens were added and energy was reduced. Using Kollman-united charge, the partial atomic charge was computed, and the prepared file was stored in PDBQT format. A test set of 22 compounds identified tentatively from PM extract in negative ion mode LC/MS/MS was prepared *via* AutoDockTools (ADT, v1.5.6) manipulating prepare_ligand4.py command and saved in PDBQT format.

Redocking of the co-crystallized ligands and virtual screening of the test set

Self-docking was performed for ligands co-crystallized with breast and ovarian cancer cell line selected proteins (PDB

Table 1. Compounds determined tentatively in *Panicum maximum* extract in negative ion mode. LC/MS-ESI/MS.

Compound	RT (min)	$[M-H]^-$	Molecular formula
(–)-Shikimic acid	1.159	173.0832	$C7H_{10}O_5$
2,5-Dihydroxybenzoic acid	1.225	153.0182	$C_7H_6O_4$
Caffeic acid	1.326	179.0571	$C_9H_8O_4$
3-(4-Hydroxyphenyl) prop-2-enoic acid	1.464	163.0388	$C_9H_8O_3$
P-hydroxybenzoic acid	1.552	136.9316	$C_7H_6O_3$
Chlorogenic acid	1.943	353.0865	$C_{16}H_{18}O_9$
3-(4-Hydroxy-3-methoxyphenyl) prop-2-enoic acid	2.020	193.0515	$C_{10}H_{10}O_4$
Kaempferol-7-neohesperidoside	4.431	593.1537	$C_{27}H_{30}O_{15}$
3,4-Dihydroxybenzoic acid	4.470	153.0182	$C_7H_6O_4$
Acacetin-7-*O*-rutinoside	4.620	591.1329	$C_{28}H_{32}O_{14}$
Daidzein-8-*C*-glucoside	4.637	415.1264	$C_{21}H_{20}O_9$
Apigenin 8-*C*-glucoside	6.074	431.0974	$C_{21}H_{20}O_{10}$
Vitexin-2″-*O*-rhamnoside	6.260	577.1900	$C_{27}H_{30}O_{14}$
Kaempferol-3-glucuronide	6.272	461.1120	$C_{21}H_{18}O_{12}$
Rhoifolin	6.869	577.1834	$C_{27}H_{30}O_{14}$
Kaempferol-3-*O*-(6-p-coumaroyl)-glucoside	8.056	593.1846	$C_{30}H_{26}O_{13}$
Luteolin-6-*C*-glucoside	10.077	447.2619	$C_{21}H_{20}O_{11}$
3,5,7-Trihydroxy-4′-methoxyflavone	10.700	299.0542	$C_{16}H_{12}O_6$
3′-Methoxy-4′,5,7-trihydroxyflavonol	12.450	315.1923	$C_{16}H_{12}O_7$
Apigenin	13.478	269.0461	$C_{15}H_{10}O_5$
Gamma-linolenic acid	19.985	277.2176	$C_{18}H_{30}O_2$
(+)-3,3′,4′,5,7-pentahydroxyflavan	20.767	289.1805	$C_{15}H_{14}O_6$

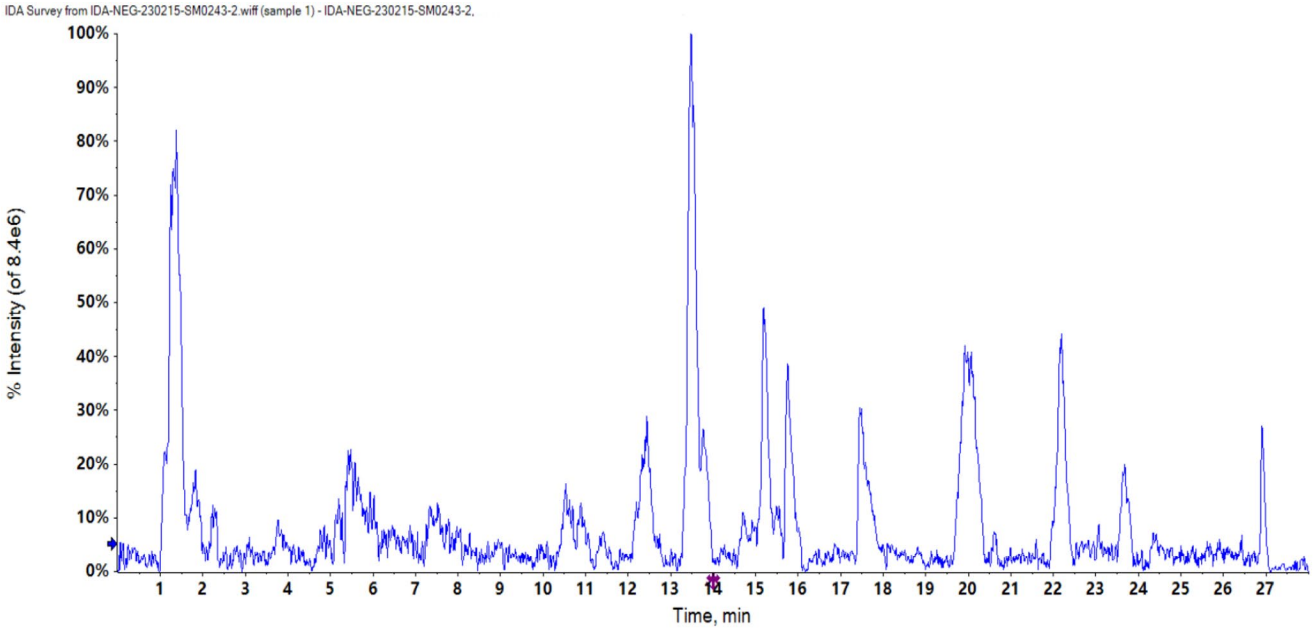

Figure 1. Total ion chromatogram of *Panicum maximum* aerial parts in negative ion mode of LC/MS-ESI/MS.

IDs: 3ERT and 5DSY, respectively) *via* AutoDock 4.2.6 to validate the docking protocol. The grid box was set to ($x = 30.010$, $y = -1.913$, and $z = 24.207$) and ($x = 17.438$, $y = 23.019$, and $z = 16.374$) for 3ERT and 5DSY active sites, respectively. The docking parameters were set to 2.500.00 energy evaluation, 100 runs number, and 150 for the size of the population based on the Lamarckian genetic algorithm [34]. The same docking protocol was used for the test set (22 compounds of PM extract). Ten binding modes were produced for each ligand with a maximum of 3 kcal/mol energy difference between each mode, and the best conformations, showing the lowest binding free energy, were retrieved. BIOVA Discovery Studio Visualizer 2021 was used to generate 2D interaction figures.

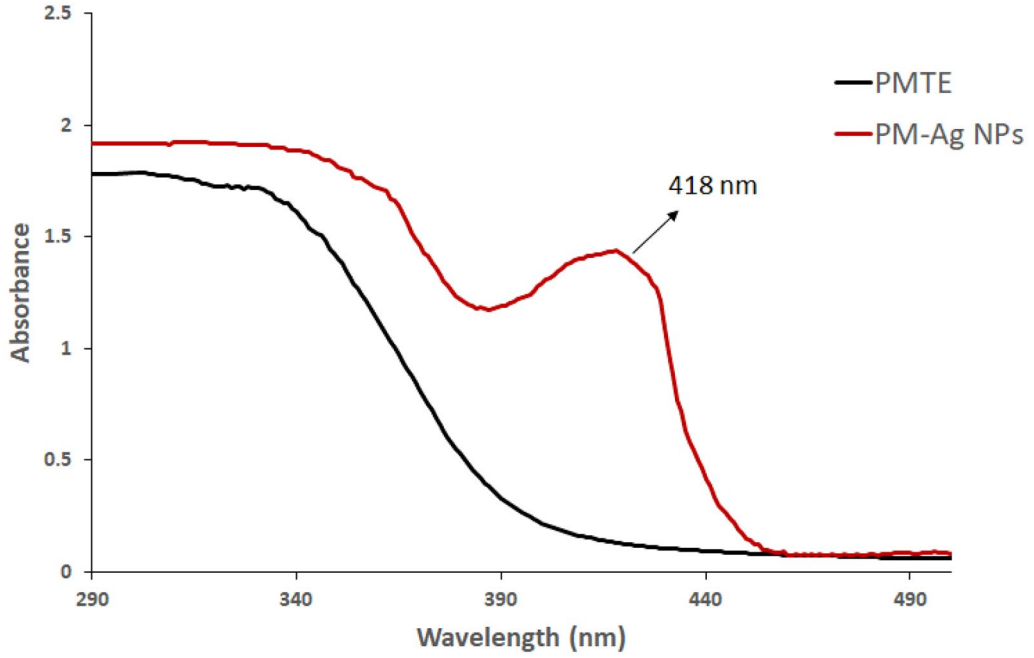

Figure 2. UV-vis spectroscopy of PM extract and PM-AgNPs.

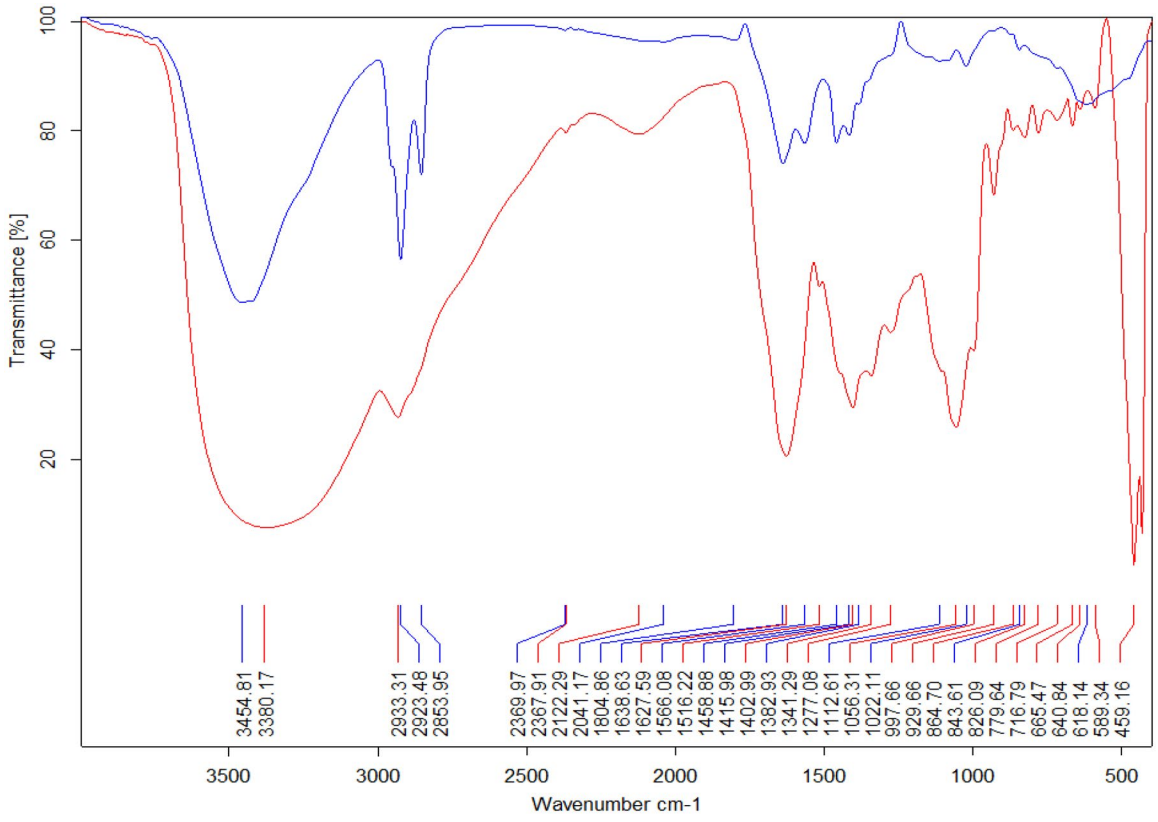

Figure 3. FTIR spectrum of PM-AgNPs (blue line) and PMTE (red line).

Results and discussion

LC/MS-ESI/MS analysis

The LC/MS-ESI/MS was employed to identify chemicals in PMTE. Several phenolics were identified, such as (shikimic acid, 2,5 dihydroxybenzoic acid, caffeic acid, chlorogenic acid, 3-(4-hydroxyphenyl) prop-2-enoic acid, 1-hydroxybenzoic acid, 3,4 dihydroxybenzoic acid, gamma-linolenic acid, and 3-(4-hydroxy-3-methoxyphenyl) prop-2-enoic acid). In addition, numerous flavonoids *O* or *C*-glycoside and some flavonoids aglycon derivatives were detected, as presented in Table 1 and Figure 1.

Characterization of the PM-AgNPs

PM-AgNPs formation

The formation of an opaque yellowish-brown colour in the reaction flask and the appearance of residue are evidence for the formation of silver nanoparticles.

UV-vis

Due to UV's selectivity for the generation of nanoparticles, UV-Vis spectroscopy provided the first characteristic of nanoparticle formation. Free electrons generate a surface plasmon resonance (SPR) absorption band [35] due to the collective oscillation of electrons in PM-AgNPs, which leads to a characteristic wavelength absorbance for each metal nanoparticle produced. The formed PM-AgNPs showed an absorbance of 418 nm (Figure 2).

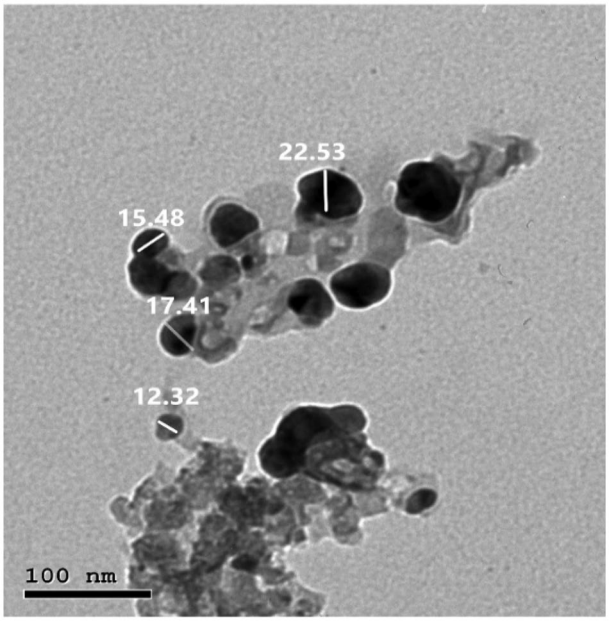

Figure 4. HR-TEM photograph of PM-AgNPs formed *via* PMTE at 100 nm.

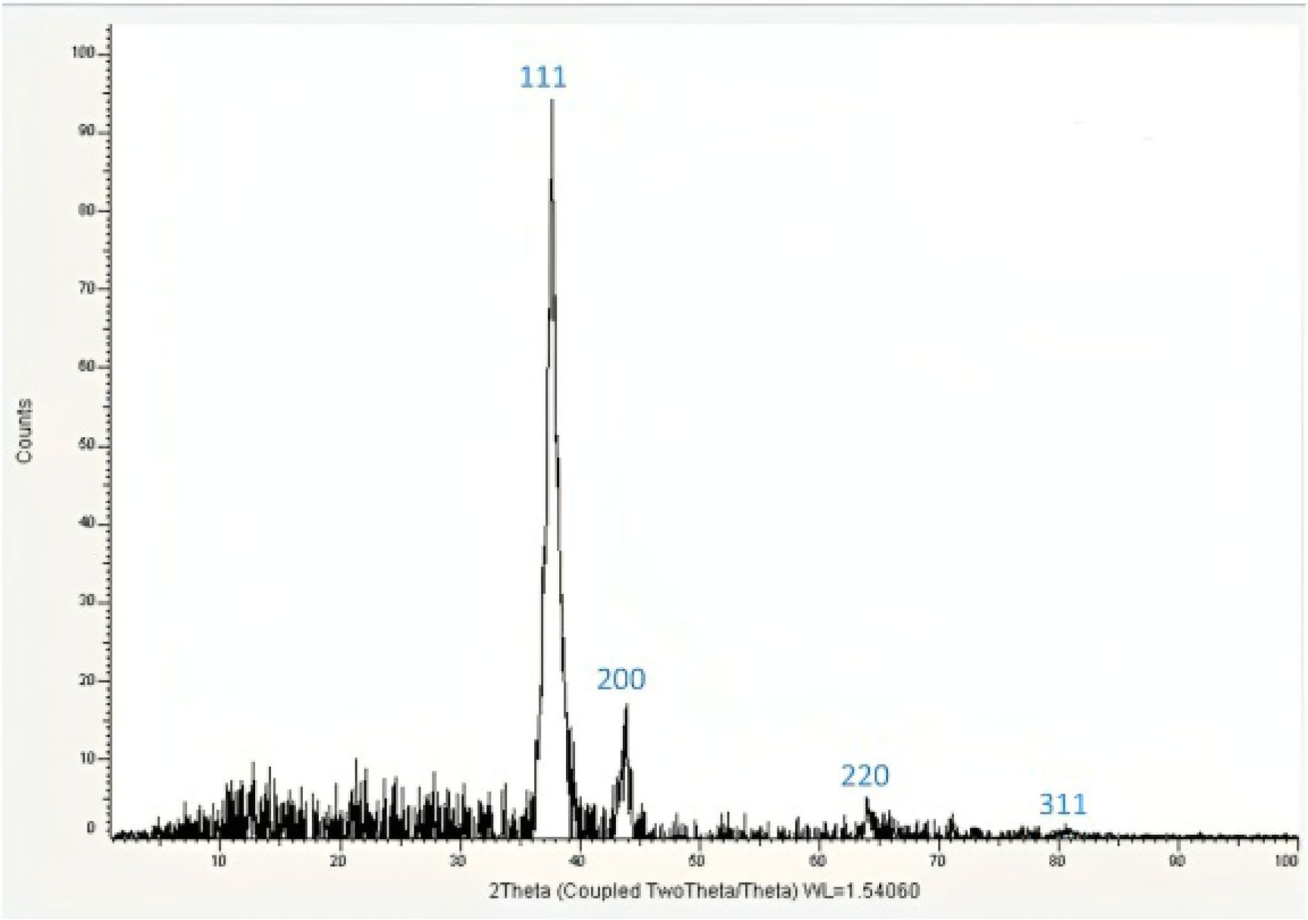

Figure 5. XRD analysis of PM-AgNPs.

FTIR

To determine which functional chemical groups of PM-AgNPs operate as reducing agents in the process of creating PM-AgNPs, FTIR spectroscopy studies were conducted.

Utilizing FTIR analysis, it was possible to identify the functional groups present in the PMTE (Figure 3). The principal transmission peaks for PMTE were found to be at 3380.17, 2933.21, 1022.11, 1627.59, and 779.64 cm^{-1}. These correspond to the stretching vibrations of O–H, glycosidic bond C–O, aliphatic C–H group, carboxylate group, and C–H alkenes, respectively.

While some of the absorbance peaks of the O–H, C–O, carboxylate, and C–H alkenes groups changed into 3454.81, 1056.31, 1638.66, and 618.14 cm^{-1}, respectively, the absorbance bands of PM-AgNPs and PMTE shown a strong resemblance.

High-resolution (HR-TEM)

The formed PM-AgNPs using PMTE as a reducing agent were assessed using a Transmission Electron Microscope HR-TEM, which declared the creation of spherical PM-AgNPs with an average particle size of 15.18 nm (Figure 4).

Zeta potential

The PM-AgNPs zeta potential peaks at −22.24 mV, signifying that the biosynthesized PM-AgNPs particles had a moderate distribution in the media and were negatively charged. In general terms, the negative sign of the zeta potential is regarded as a positive sign of physical stability, with a stronger repulsion force providing the best possible dispersibility of nanoparticles (Figure 6).

Table 2. The IC_{50} (µg) of PMTE and biosynthesized PM-AgNPs against different human solid tumour cells.

	IC_{50} (µg)		
Compounds	MCF-7	A549	SKOV 3
PMTE	2.5 ± 0.5	79.4 ± 3.2	9.3 ± 0.8
PM-AgNPs	0.13 ± 0.015	13 ± 3.2	3.5 ± 0.5

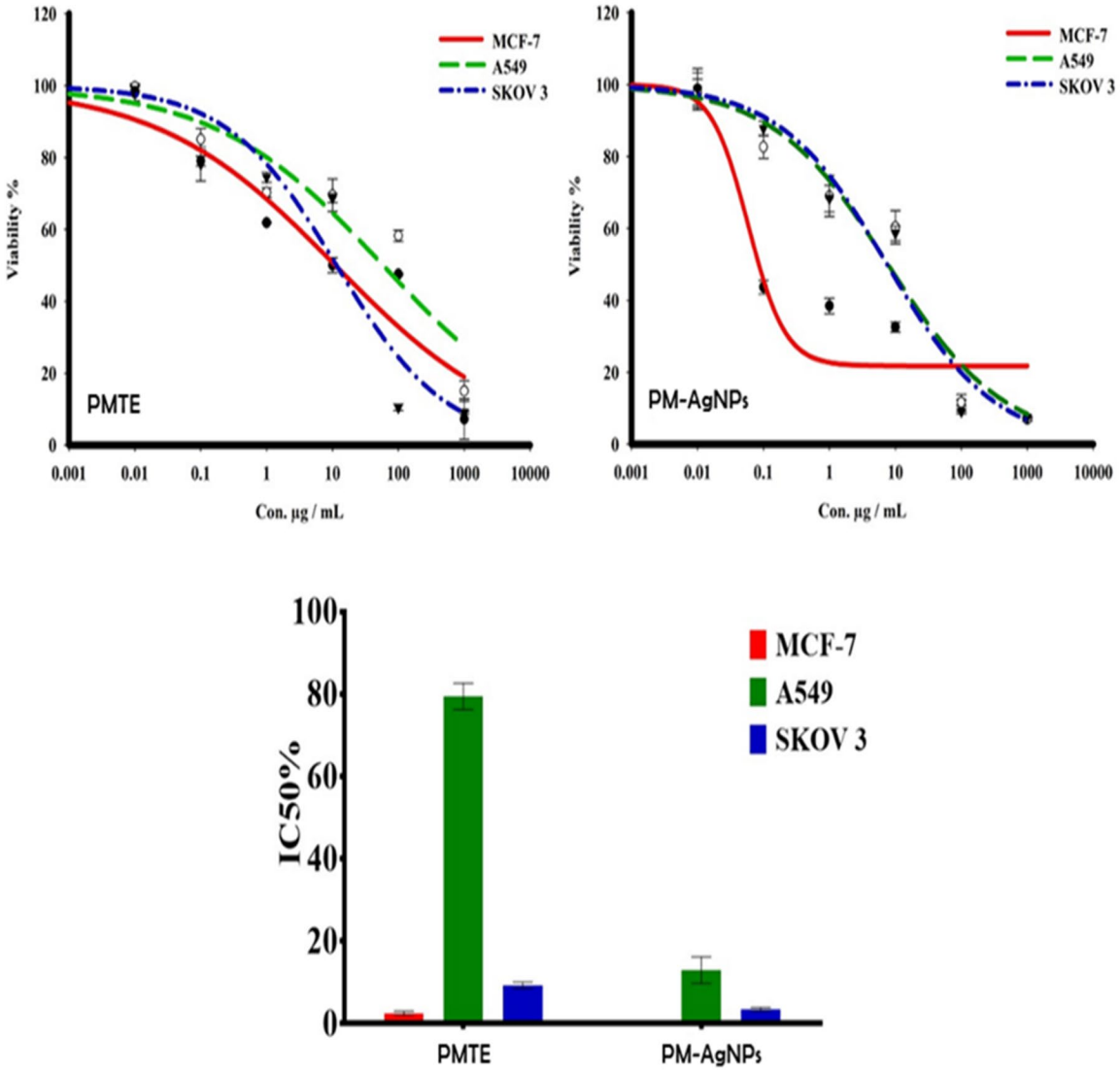

Figure 6. The toxicity response of PMTE and PM-AgNPs to cancerous cells MCF-7, A549, and SKOV3. For 72 h, cells were incubated with variable concentrations of materials. SRB staining was used to determine cell viability.

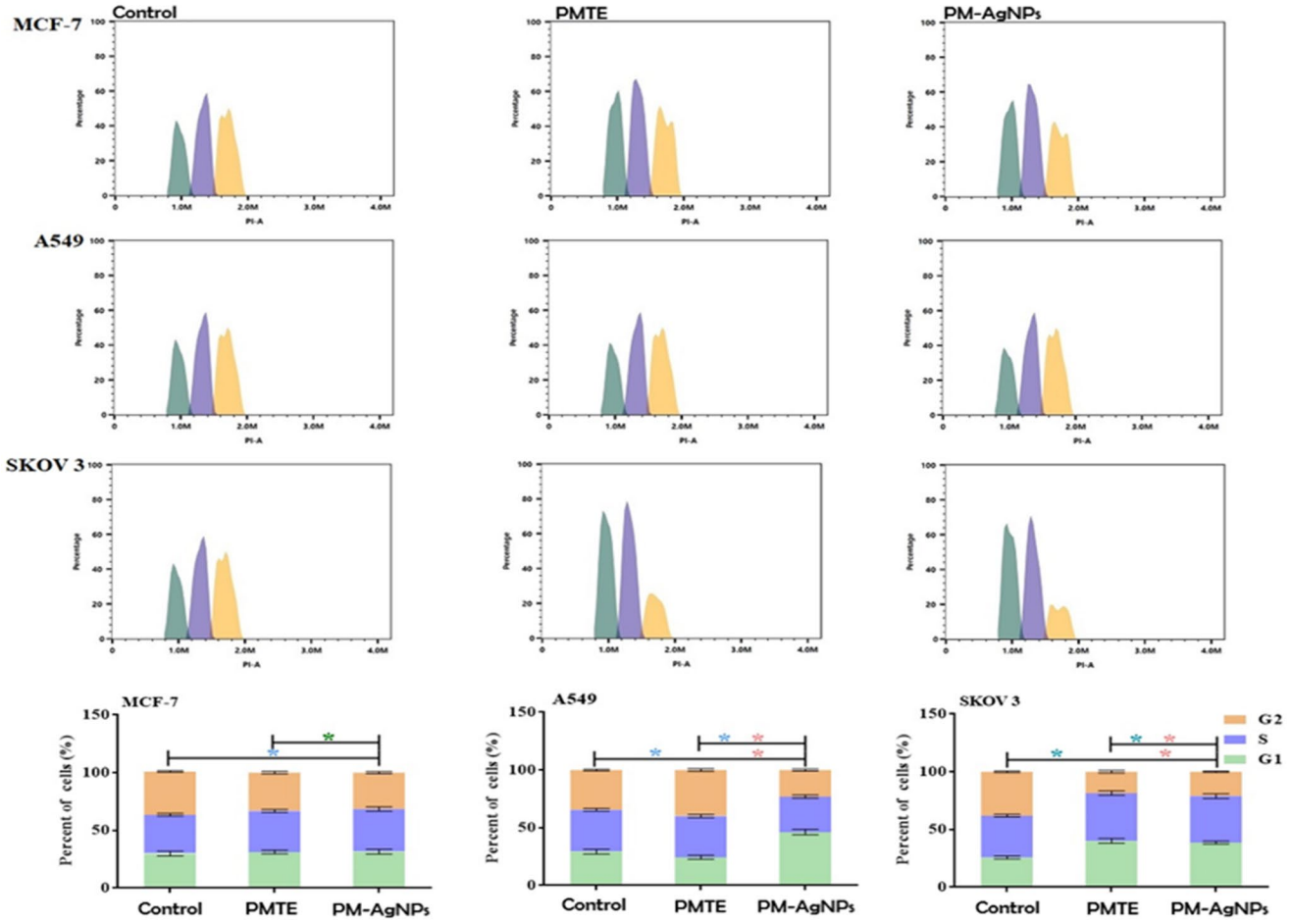

Figure 7. Effect of PMTE and PM-AgNPs on cell cycle distributions of MCF-7, A549, and SKOV3 cells. Cell cycle distribution was determined using DNA cytometry analysis after exposure to PMTE and PM-AgNPs for 48 h. Data are presented as the mean ± *SD*; $n = 3$; * $p < 0.5$ and ** $p < 0.01$.

XRD

The crystallography nature of the formed PM-AgNPs was evaluated by X-ray (XRD). Herein, the PM-AgNPs exhibited peaks with 2θ values at 38.262, 44.473, 64.714, 77.737, 81.910, corresponding to (111, 200, 220, 311) in the same order (Figure 5).

Antioxidant activity

This study used radical scavenging and metal-reducing assays to recognize PMTE antioxidant effects. ABTS test was employed as a radical scavenging assay. PMTE has an antioxidant activity of 805.976 ± 57.351 µM Trolox equivalents (TE)/mg. The FRAP test was utilized as a metal-reduction assay, and the PMTE activity was 243.359 ± 22.058 µM TE/mg. Numerous abiotic stresses trigger the overproduction of reactive oxygen species (ROS) that are highly toxic and reactive. These ROS are known to cause damage to carbohydrates, DNA, lipids, and proteins, and build oxidative stress, and results in the induction of various diseases [36]. To resolve this issue, antioxidants molecules have gained significant attention to scavenge these free radicals and ROS [37,38]. However, poor absorption ability, difficulty crossing the cell membranes, and degradation of these antioxidants during delivery are the few challenges associated with natural and synthetic antioxidants that limit their bioavailability. Thus, NPs have gained great attention as antioxidants [39].

Cytotoxic activity

The cytotoxic potentials of PMTE and PM-AgNPs were tested against human cancer cells MCF-7, A549, and SKOV3, implying SRB assay. At concentrations ranging from 0.01 to 1000 g, the SRB assay was used to determine the *in vitro* cytotoxic activities tested against the MCF-7, A549, and SKOV 3 cancer cell lines. The compounds studied displayed a wide range of cytotoxic properties against cancerous cells. The cytotoxic properties of PM-AgNPs on MCF-7 and SKOV3 were the strongest, with IC_{50}s of 0.13 ± 0.015 and 3.5 ± 0.5 g/ml, respectively, compared to the effect of PMTE on the same tumour cells (MCF-7) and SKOV 3, with IC_{50}s of 2.5 ± 0.5 and 9.3 ± 0.8 µg/mL, respectively (Table 2 and Figure 6). Also, PM-AgNPs has a promising toxicological effect on human lung cancer cells A549, with an IC_{50} of 13 ± 3.2 µg/mL compared to PMTE, has a week of cytotoxicity at an IC_{50} of 79.4 ± 3.2 µg/mL.

The effect on the cell cycle distribution of solid tumour cells

The tumour cell cycle's phases were monitored to examine anticancer effects. Therefore, following 48 h of treatment in

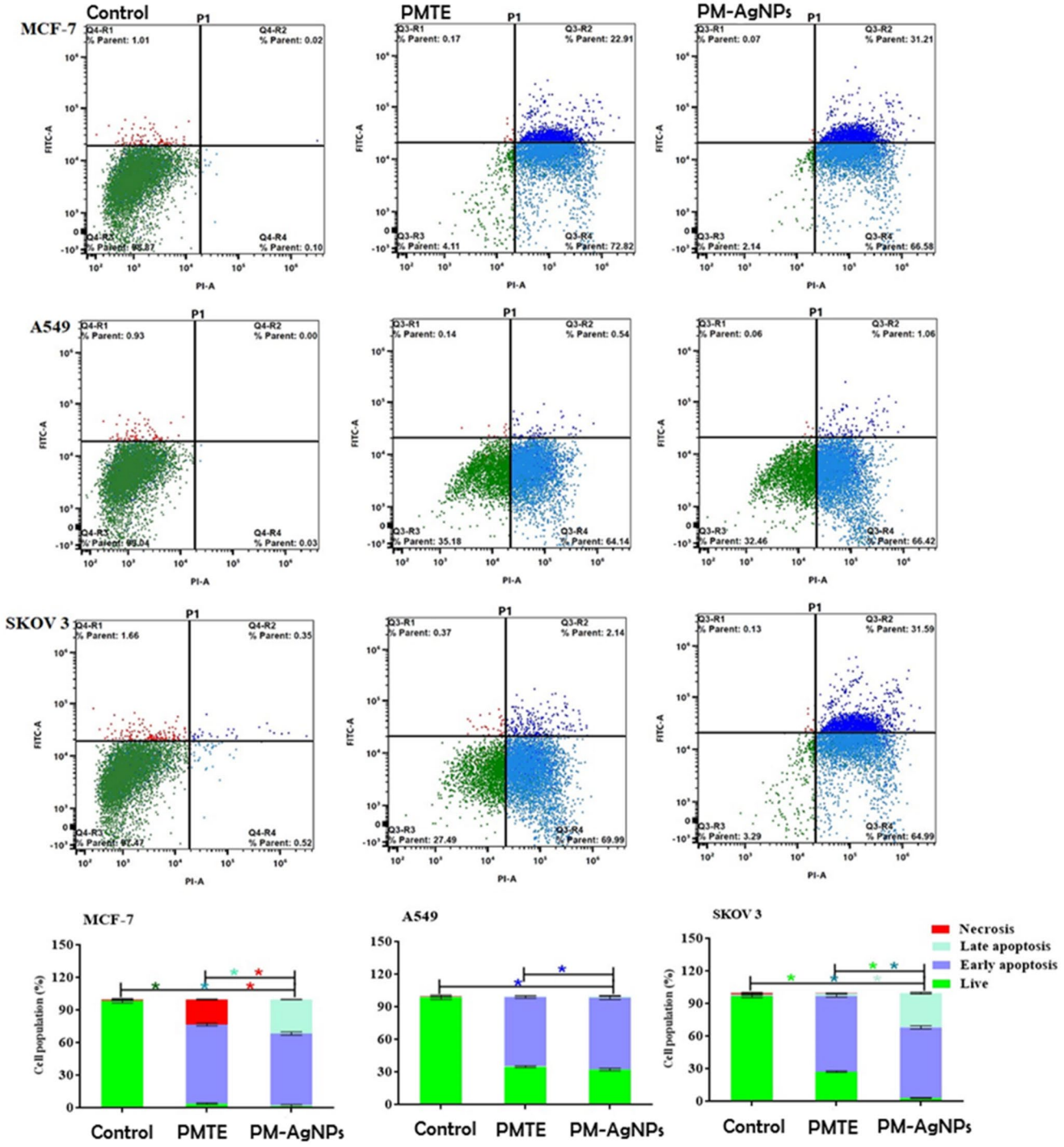

Figure 8. Apoptosis/necrosis assessment of PMTE and PM-AgNPs against MCF-7, A549, and SKOV3 subjected to previous treatment for 48 h, and apoptosis/necrosis quantified using flow cytometry. Data are presented as the mean ± *SD*; $n = 3$; *$p < 0.05$, **$p < 0.01$ and ***$p < 0.001$.

cancer cells, the effects of PMTE and PM-AgNPs on the distribution of cell cycle phases in MCF-7, A549, and SKOV3 cells were investigated using flow cytometry. Figure 7 illustrates that the treatment with PM-AgNPs resulted in a substantial increase of 37 ± 1.4% in the ratio of MCF-7 cells arrested in the S phase. Conversely, PMTE had no discernible impact on the cell cycle distributions of MCF-7 cells in the cell phases when compared to untreated cells. In A549 cells treated with PM-AgNPs, G1 was arrested by 46.2 ± 1.1% compared to the cell control. In the meanwhile, after receiving PMTE treatment, the percentage of G1 and S phases in SKOV3 cells grew and stopped at 40.1 ± 0.8% and 41.5 ± 0.5, respectively. Additionally, G1 and S phases were influenced by 38.7 ± 1.1% and 40.2 ± 0.2, respectively, after receiving PM-AgNPs treatment. Previous studies revealed the efficiency of *Siberian ginseng*, green synthesized AgNPs in the cytotoxicity in the MCF7 cell lines [40]. Potential anticancer activity was also shown in triggering cell death through necrosis and apoptosis both by AgNPs synthesized using leaf extract of *Andrographis echioides*, and its bio-cytotoxicity was observed by the transfer of the electron from molecular oxygen [41].

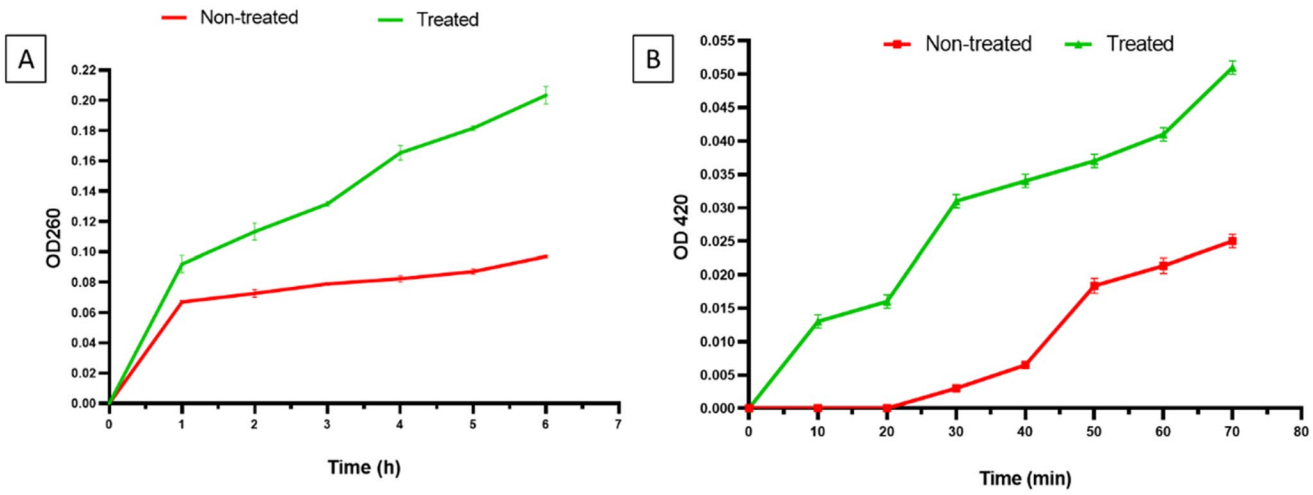

Figure 9. (A) Membrane integrity and (B) membrane permeability of a representative isolate after treatment with PM-AgNPs.

Table 3. Influence of PM-AgNPs on the biofilm formatting ability of *S. aureus* isolates.

	The number of isolates	
Biofilm formation	Before treatment	After treatment
Non-forming	3	5
Weak	2	8
Moderate	4	1
Strong	7	2

Table 4. Docking Δ*G* scores of 22 compounds of PM extract on both 3ERT and 5DSY active pockets.

	Δ*G* (Kcal/mol)	
Compound	3ERT	5DSY
Native	−9.4345	−9.1171
(−)-Shikimic acid	−4.9929	−5.1689
2,5-Dihydroxybenzoic acid	−4.9160	−4.9784
Caffeic acid	−5.1578	−5.2014
3-(4-Hydroxyphenyl) prop-2-enoic acid	−4.8705	−5.0234
P-hydroxybenzoic acid	−4.5571	−4.4946
Chlorogenic acid	−7.2776	−7.0284
3-(4-Hydroxy-3-methoxyphenyl) prop-2-enoicacid	−5.7931	−5.3781
Kaempferol-7-neohesperidoside	−9.0772	−8.2378
3,4-Dihydroxybenzoic acid	−4.7028	−4.9191
Acacetin-7-*O*-rutinoside	−9.0515	−9.4145
Daidzein-8-*C*-glucoside	−7.3423	−7.0192
Apigenin 8-*C*-glucoside	−7.4441	−7.8696
Vitexin-2″-*O*-rhamnoside	−7.8526	−8.1479
Kaempferol-3-glucuronide	−8.0089	−7.3913
Rhoifolin	−9.5071	−9.1882
Kaempferol-3-*O*-(6-p-coumaroyl)-glucoside	−8.3252	−9.3689
Luteolin-6-*C*-glucoside	−7.0585	−7.6572
3,5,7-Trihydroxy-4′-methoxy flavone	−6.2236	−6.2766
3′-Methoxy-4′,5,7-trihydroxy flavonol	−6.6815	−6.5435
Apigenin	−6.5176	−5.9616
Gamma-linolenic acid	−7.2253	−7.1031
(+)-3,3′,4′,5,7-pentahydroxyflavan	−6.3937	−6.0758

Evaluation of cell apoptosis using Annexin V-FITC

To differentiate between cells passing through apoptosis, or programmed cell death, and cells dying by necrosis, or non-programmed cell death, in MCF-7, A549, and SKOV3 cells, annexin V-FITC/PI labelling was performed in accordance with a flow cytometer (Figure 8). After treating MCF-7 cells with PMTE and PM-AgNPs, there was a 73 ± 3.32 and 97.79 ± 1.61% increase in the number of apoptotic cells, respectively. As well as in SKOV3 after treatment with (PMTE and PM-AgNPs) of 72.14 ± 2.41 and 96.6 ± 1.91%, respectively, compared to the cell control. Furthermore, when A549 cancer cells were treated with PMTE and PM-AgNPs, there was a significant increase in apoptotic cells of 64.68 ± 1.91 and 67.48 ± 2.2%, respectively, relative to the cell control.

Antibacterial action

The antibacterial potential of PM-AgNPs was revealed by the agar well diffusion method. PM-AgNPs displayed antibacterial activity towards the tested *S. aureus* isolates as inhibition zones were displayed around the wells. The MIC values ranging from 64 to 512 µg/mL (Table S1).

Influence on the membrane properties

PM-AgNPs were found to affect the membrane integrity and membrane permeability of 50 and 43.75% of the tested isolates, respectively (Figure 9).

Affecting the membrane properties is a common target for many antimicrobials [9]. The bacterial membrane is an integral part of the bacterial cell, preserving its interior constituents. Therefore, affecting it would have detrimental impacts on the bacterial cell and could lead to bacterial death [42,43].

Antibiofilm action

PM-AgNPs significantly impacted the tested isolates' capacity to form biofilms, as evidenced by the drop in the proportion of strong and moderate biofilm-forming isolates from 68.75 to 18.75% (Table 3). Biofilm is an important virulence factor for many bacterial species, enabling the bacterial cells to communicate. The antibiotic resistance genes could be transferred among the bacterial cells in biofilm [44,45]. In the current investigation, PM-AgNPs decreased the biofilm formation of the tested isolates, comparable to other findings of earlier studies [8,46].

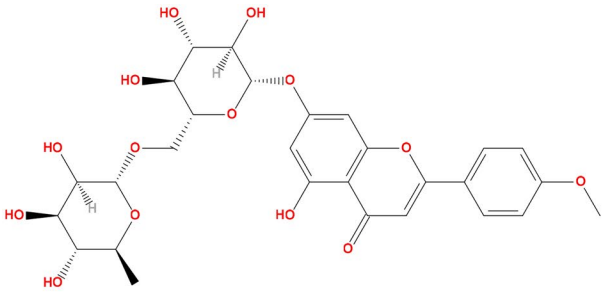

Acacetin-7-*O*-rutinoside

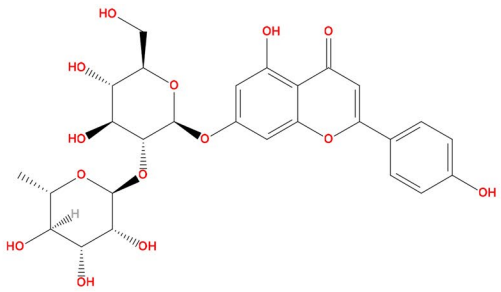

Rhoifolin

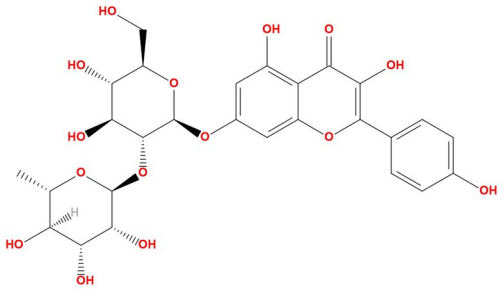

Kaempferol-7-neohesperidoside

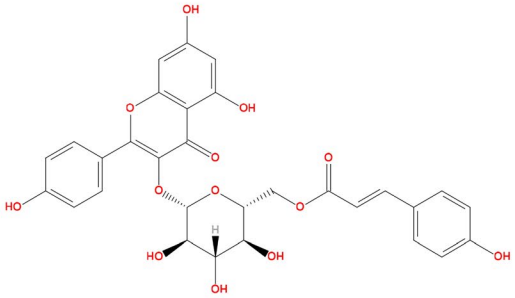

Kaempferol-3-*O*-(6-p-coumaroyl)-glucoside

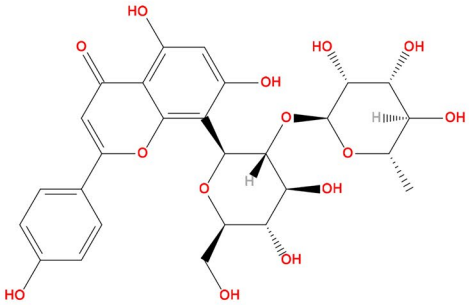

Vitexin-2"-*O*-rhamnoside

Figure 10. 2D chemical structure of the best 5 hits resulted from docking on ERα and PARP receptors active site.

In silico study

Protein and test set preparation for docking

The co-crystallized ligand underwent self-docking to verify the docking procedure. Table S2 illustrates how self-docking of the co-crystallized ligands yields poses and interactions that are exactly like those that have been documented.; RMSD = 0.2501 and 1.1536 Å, $\Delta G = -9.4345$ and −9.1171 Kcal/mol, for ERα and PARP, respectively. 4-hydroxytamoxifen (ERα co-crystallized ligand) showing high binding affinity towards its active pocket with 4 main interactions: H-bond with Glu 353, ionic interaction with Asp 351, pi-sulfur interaction with Met 343 and amide-pi stacking with Leu 346. For PARP, 5DSY co-crystallized ligand was able to form 3 H-bonds with Arg 431, Gly 429, and Gly 424, in addition to forming 2 pi-pi stacking interactions with both try 460 and Tyr 449.

Virtual screening of the 22 compounds in a test set on 2 PDB IDs demonstrates that all 22 compounds have good binding affinities towards both receptors ($-4.5571 < \Delta G < -9.5071$ and $-4.4946 < \Delta G < -9.4145$ Kcal/mol for 3ERT and 5DSY, respectively) as revealed in Table 4. Five compounds of them: Acacetin-7-*O*-rutinoside, Rhoifolin, Kaempferol-7-neohesperidoside, Kaempferol-3-*O*-(6-p-coumaroyl)-glucoside and Vitexin-2″-*O*-rhamnoside possess the highest binding affinity against both receptors comparable to their native co-crystallized ligands with binding free energy ($-8.3252 < \Delta G < -9.5071$ and $-8.4145 < \Delta G < -9.4145$ Kcal/mol for 3ERT and 5DSY, respectively) and their chemical structure is displayed in Figure 10.

The 2D interactions of the best five hits against both receptors were studied (Figures 11 and 12). Regarding ER α, one main interaction, pi-sulfur interaction with Met 343, is maintained in 4 hits out of 5 hits in addition to the

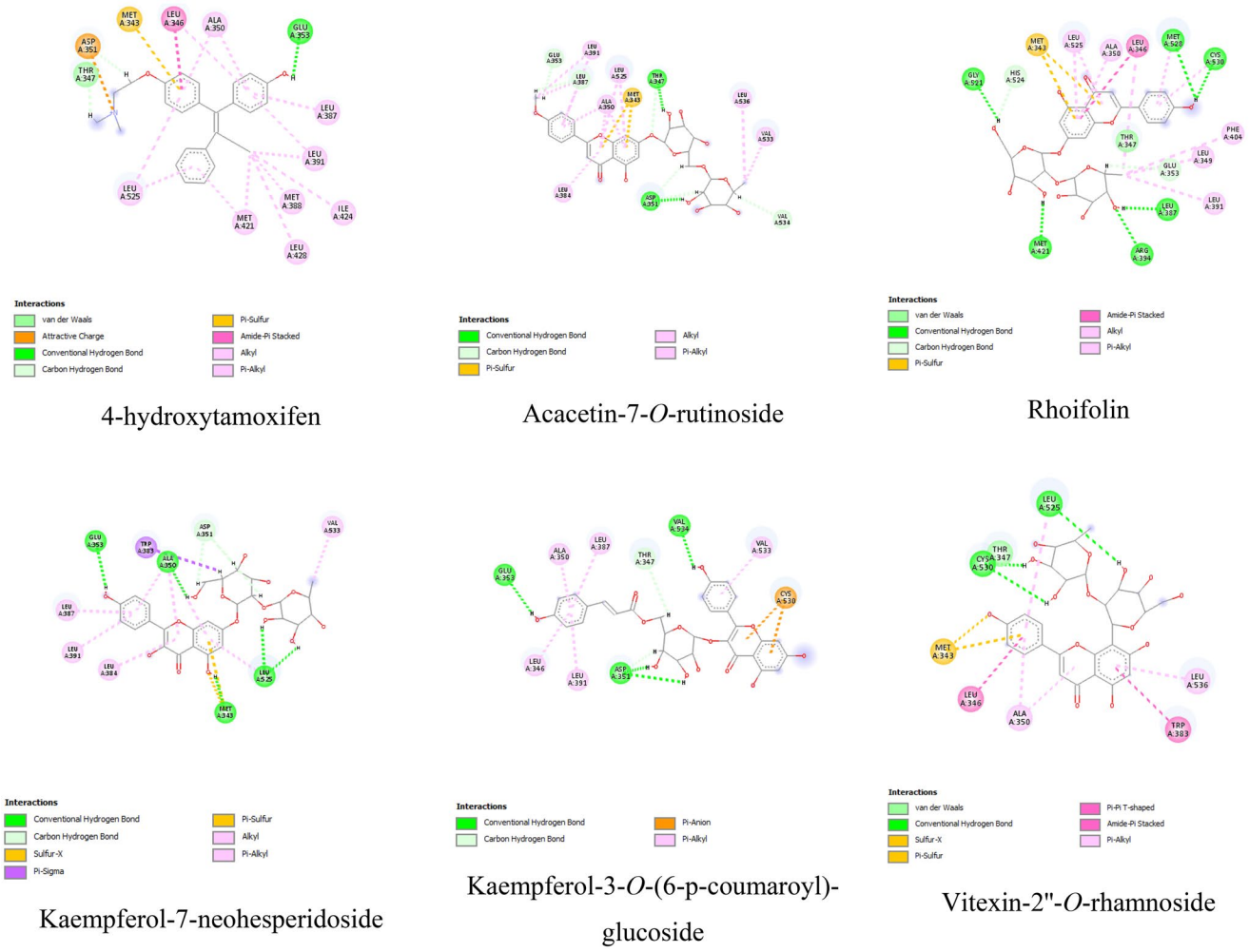

Figure 11. 2D interactions 4-hydroxytamoxifen (native ligand) and the best five hits docked on ERα (PDB ID: 3ERT).

native ligand. Also, Leu 346 appeared to be the main amino acid involved in the interaction. It was involved in interacting with the native ligand, forming amide-pi interaction in addition to 2 of the top hits; Rhoifolin and Vitexin-2″-*O*-rhamnoside, forming amide-pi and pi-pi interactions, respectively. Besides that, Kaempferol-3-*O*-(6-p-coumaroyl)-glucoside created a pi-anion interaction with Cys 530. Generally, the native ligand and the best 5 hits can form at least one H-bond bond with pocket amino acids (Figure 10).

For PARP in ovarian cancer, at least one of 3 pi-pi interactions is present between either the native ligand or 5 best hits and the receptor active sites. Pi-pi interaction takes place with Tyr 460, Tyr 449 and His 415 in rhoifolin, kaempferol-7-neo hesperidoside and kaempferol-3-*O*-(6-p-coumaroyl)-glucoside. for vitexin-2″-*O*-rhamnoside, there were only 2 pi-pi interactions with Tyr 460 and His 415 and only one pi-pi interaction against Acacetin-7-*O*-rutinoside and the native ligand with Tyr 442 and Tyr 460, respectively. In addition to pi-pi stacking, all 6 ligands possess 2–3 H-bonds and maintain a main H-bond with Arg 431 as a main amino acid involved in increasing the binding affinity towards PARP active pocket.

A deep insight into the chemical structure of the five hits, we found that all of them share a kaempferol structure involved in the main interactions among the active sites of both receptors. Kaempferol, a flavonoid antioxidant, is previously reported to have a cytotoxic effect against tumours, especially breast cancer, by inhibiting tumour cell growth, inducing their apoptosis, and inhibiting migration and invasion [47–49]. It also inhibited ovarian tumour cell proliferation by upregulating p53, Bad, and Bax proteins (pro-apoptotic and anti-apoptotic proteins) [50]. Accordingly, the kaempferol structure is suggested to be the main backbone responsible for the cytotoxic activity of *Panicum maximum* on MCF-7 and SKOV 3.

Conclusion

PM-AgNPs revealed antibacterial potential towards *S. aureus* bacteria with MIC values that ranged from 64 to 512 µg/mL. The nanoparticles exhibited a reduction in the membrane integrity as well as an increase in the permeability of the tested bacteria. In addition, using crystal violet assay, PM-AgNPs showed antibiofilm activity against the biofilm-forming *S. aureus* isolates. PM-AgNPs revealed cytotoxic properties on MCF-7 and SKOV 3, with IC_{50}s of 0.13 ± 0.015 and 3.5 ± 0.5 g/ml, respectively. The cell cycle analysis using flow cytometry for

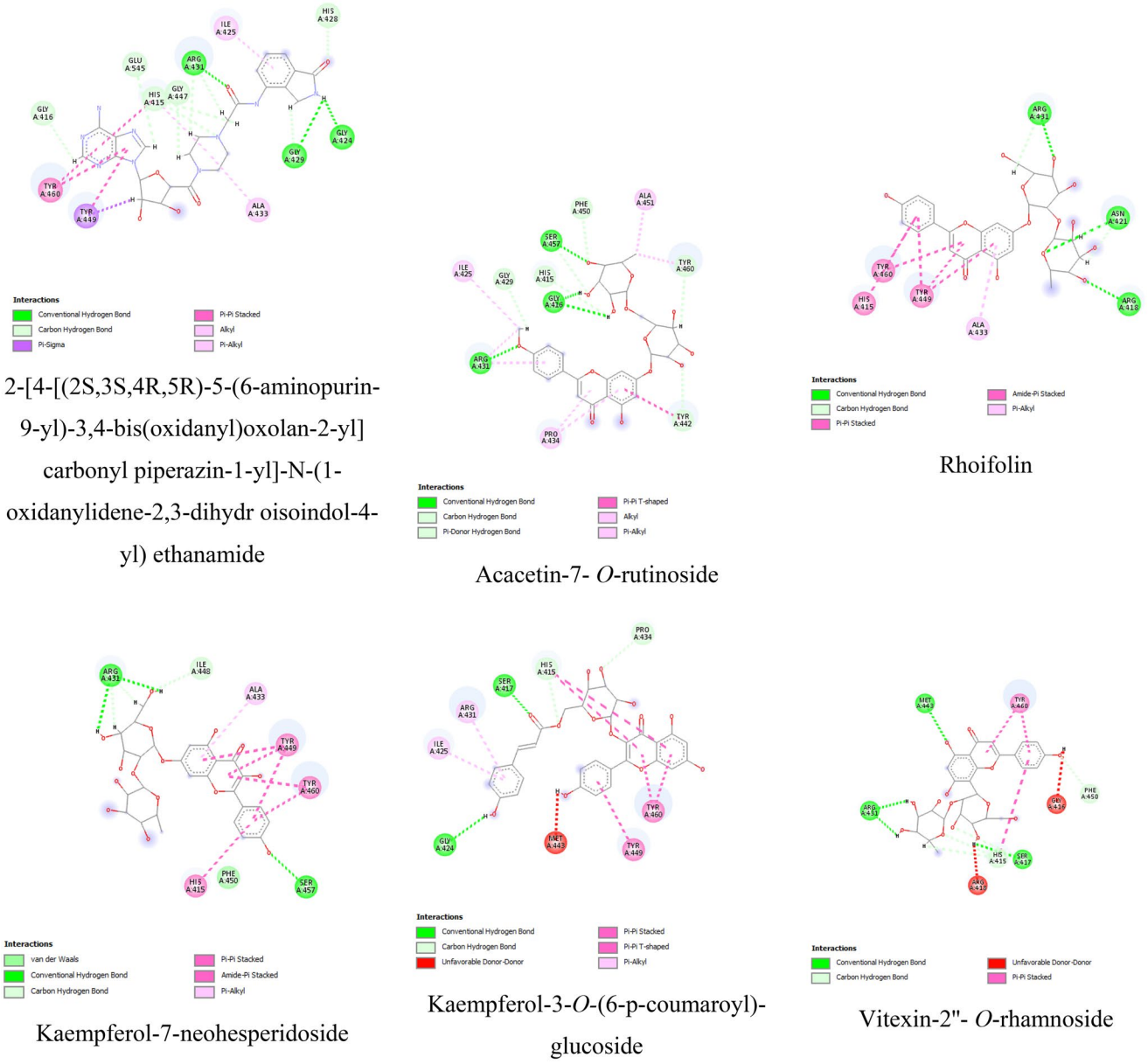

Figure 12. 2D interactions native ligand and the best five hits docked on PARP (PDB ID: 5DSY).

the three cell lines revealed that the increase in the population of the apoptotic cells was 97.79 ± 1.61 and 96.6 ± 1.91%, respectively. Consequently, more future studies are required to investigate the potential anticancer, antioxidant, and antibacterial activities of PM-AgNPs *in vivo*.

Author contributions

Conceptualization, Heba W. Alhamdi, Fatma Alzahraa Mokhtar, Ali A. Shati, Serag Eldin I. Elbehairi, Hanan Khalaf Anazi, Lamiaa I. Fahmy, Mohammad Y. Alfaifi, and Sherif Ashraf Fahmy, Nabil Selim; data curation, Serag Eldin I. Elbehairi, Hanan Khalaf Anazi, and Sherif Ashraf Fahmy; investigation, Fatma Alzahraa Mokhtar, Engy Elekhnawy, Walaa A. Negm, Serag Eldin I. Elbehairi, Lamiaa I. Fahmy, Mohammad Y. Alfaifi, and Sherif Ashraf Fahmy; resources, Heba W. Alhamdi, Mohammad Y. Alfaifi, and Hanan Khalaf Anazi; methodology, Nabil Selim and Engy Elekhnawy; software, Fatma Alzahraa Mokhtar and Afnan Hassan; supervision, Seham S. Elhawary, Fatma Alzahraa Mokhtar, and Sherif Ashraf Fahmy; validation, Ali A. Shati, Walaa A. Negm, and Sherif Ashraf Fahmy; writing–original draft, Engy Elekhnawy, Walaa A. Negm, Heba W. Alhamdi, Ali A. Shati, Serag Eldin I. Elbehairi, Lamiaa I. Fahmy, Mohammad Y. Alfaifi, Afnan Hassan, and Sherif Ashraf Fahmy; writing–review and editing, Seham S. Elhawary, Fatma Alzahraa Mokhtar, and Sherif Ashraf Fahmy.

Disclosure statement

No potential conflict of interest was reported by the author(s).

Funding

The authors thank the Deanship of Scientific Research at King Khalid University for funding this work through large Groups (Project under grant number R.G.P.2/217/44).

ORCID

Fatma Alzahraa Mokhtar http://orcid.org/0000-0002-6909-7440
Engy Elekhnawy http://orcid.org/0000-0001-8287-1026
Walaa A. Negm http://orcid.org/0000-0003-0463-8047
Sherif Ashraf Fahmy http://orcid.org/0000-0003-3056-8281

Data availability statement

All the data for this research are available in the main manuscript and associated Supplementary File.

References

[1] Sedky NK, Mahdy NK, Abdel-Kader NM, et al. Facile sonochemically-assisted bioengineering of titanium dioxide nanoparticles and deciphering their potential in treating breast and lung cancers: biological, molecular, and computational-based investigations. RSC Adv. 2024;14(12):8583–8601. doi: 10.1039/d3ra08908h 38487521.
[2] Benabderrahim MA, Elfalleh W. Forage potential of non-native Guinea grass in north African agroecosystems: genetic, agronomic, and adaptive traits. Agronomy. 2021;11(6):1071.
[3] de Sousa ACB, Jank L, de Campos T, et al. Molecular diversity and genetic structure of Guinea grass (*Panicum maximum* Jacq.), a tropical pasture grass. Trop Plant Biol. 2011;4:185–202.
[4] Mokhtar FA, Selim NM, Elhawary SS, et al. Green biosynthesis of silver nanoparticles using *Annona glabra* and *Annona squamosa* extracts with antimicrobial, anticancer, apoptosis potentials, assisted by *in silico* modeling, and metabolic profiling. Pharmaceuticals. 2022;15(11):1354.
[5] Ritacco I, Al Assy M, Abd El-Rahman MK, et al. Hydrolysis in acidic environment and degradation of satraplatin: a joint experimental and theoretical investigation. Inorg Chem. 2017;56(10):6013–6026. doi: 10.1021/acs.inorgchem.7b00945.
[6] Youness RA, Al-Mahallawi AM, Mahmoud FH, et al. Oral delivery of psoralidin by mucoadhesive surface-modified bilosomes showed boosted apoptotic and necrotic effects against breast and lung cancer cells. Polymers. 2023;15(6):1464. doi: 10.3390/polym15061464.
[7] Fahmy SA, Ramzy A, Saleh BM, et al. Stimuli-responsive amphiphilic pillar[*n*]arene nanovesicles for targeted delivery of cancer drugs. ACS Omega. 2021;6(40):25876–25883. doi: 10.1021/acsomega.1c04297.
[8] Swidan NS, Hashem YA, Elkhatib WF, et al. Antibiofilm activity of green synthesized silver nanoparticles against biofilm associated enterococcal urinary pathogens. Sci Rep. 2022;12(1):3869. doi: 10.1038/s41598-022-07831-y.
[9] Reygaert WC. An overview of the antimicrobial resistance mechanisms of bacteria. AIMS Microbiol. 2018;4(3):482–501. doi: 10.3934/microbiol.2018.3.482.
[10] Tong SY, Davis JS, Eichenberger E, et al. Staphylococcus aureus infections: epidemiology, pathophysiology, clinical manifestations, and management. Clin Microbiol Rev. 2015;28(3):603–661. doi: 10.1128/CMR.00134-14.
[11] Tam K, Torres V. *Staphylococcus aureus* secreted toxins & extracellular enzymes Kayan. Physiol Behav. 2016;176:139–148.
[12] Albalawi MA, Hafez AM, Elhawary SS, et al. The medicinal activity of lyophilized aqueous seed extract of *Lepidium sativum* L. in an androgenic alopecia model. Sci Rep. 2023;13(1):7676.
[13] Kunwar S, Roy A, Bhusal U, et al. Bio-fabrication of Cu/Ag/Zn nanoparticles and their antioxidant and dye degradation activities. Catalysts. 2023;13(5):891.
[14] Azzazy HMES, Sawy AM, Abdelnaser A, et al. *Peganum harmala*-alkaloids and tannic acid encapsulated in PAMAM dendrimers: improved anticancer activities as compared to doxorubicin. ACS Appl Polym Mater. 2022;4(10):7228–7239.
[15] Azzazy HMES, Abdelnaser A, Al Mulla H, et al. Essential oils extracted from *Boswellia sacra* Oleo gum resin loaded into PLGA–PCL nanoparticles: enhanced cytotoxic and apoptotic effects against breast cancer cells. ACS Omega. 2022;8(1):1017–1025. doi: 10.1021/acsomega.2c06390.
[16] Idris DS, Roy A. Antioxidant and dye degradation activity of green synthesized silver-iron oxide (Ag-Fe_2O_3) bimetallic nanoparticles. Nano-Struct Nano-Objects. 2024;38:101142.
[17] Walunj P, Roy A, Jadhav V, et al. Polyol-mediated zinc oxide nanoparticles using the refluxing method as an efficient photocatalytic and antimicrobial agent. Front Bioeng Biotechnol. 2023;11:1177981. doi: 10.3389/fbioe.2023.1177981.
[18] Alherz FA, Negm WA, Elekhnawy E, et al. Silver nanoparticles prepared using *Encephalartos laurentianus* De Wild leaf extract have inhibitory activity against *Candida albicans* clinical isolates. J Fungi. 2022;8(10):1005.
[19] Wu Y, Yin Z, Qie X, et al. Interaction of soy protein isolate hydrolysates with cyanidin-3-O-glucoside and its effect on the *in vitro*-antioxidant capacity of the complexes under neutral condition. Molecules. 2021;26(6):1721. doi: 10.3390/molecules26061721.
[20] El-Hawary SS, El-Hefnawy HM, Osman SM, et al. Antioxidant, anti-inflammatory and cytotoxic activities of *Jasminum multiflorum* (Burm. F.) Andrews leaves towards MCF-7 breast cancer and HCT 116 colorectal cell lines and identification of bioactive metabolites. Anticancer Agents Med Chem. 2021;21(18):2572–2582. doi: 10.2174/1871520621666210901103440.
[21] Nallusamy S, Mannu J, Ravikumar C, et al. Exploring phytochemicals of traditional medicinal plants exhibiting inhibitory activity against main protease, spike glycoprotein, RNA-dependent RNA polymerase and non-structural proteins of SARS-CoV-2 through virtual screening. Front Pharmacol. 2021;12:1704.
[22] Nunez R. DNA measurement and cell cycle analysis by flow cytometry. Curr Issues Mol Biol. 2001;3(3):67–70.
[23] Wlodkowic, D., Skommer, J., Darzynkiewicz, Z. Flow Cytometry-Based Apoptosis Detection. In: Erhardt, P., Toth, A. (eds) Apoptosis. Methods in Molecular Biology, Humana Press: Totowa, NJ; 2009. Vol. 559, doi: 10.1007/978-1-60327-017-5_2.
[24] Fahmy SA, Sedky NK, Ramzy A, et al. Green extraction of essential oils from *Pistacia lentiscus* resins: encapsulation into niosomes showed improved preferential cytotoxic and apoptotic effects against breast and ovarian cancer cells. J Drug Deliv Sci Technol. 2023;87:104820.
[25] Kovács R, Erdélyi L, Fenyvesi F, et al. Concentration-dependent antibacterial activity of chitosan on *Lactobacillus plantarum*. Pharmaceutics. 2023;15(1):18.
[26] Elekhnawy E, Sonbol F, Abdelaziz A, et al. An investigation of the impact of triclosan adaptation on *Proteus mirabilis* clinical isolates from an Egyptian university hospital. Braz J Microbiol. 2021;52(2):927–937. doi: 10.1007/s42770-021-00485-4.
[27] Sonbol FI, El-Banna TE, Abd El-Aziz AA, et al. Impact of triclosan adaptation on membrane properties, efflux and antimicrobial resistance of *Escherichia coli* clinical isolates. J Appl Microbiol. 2019;126(3):730–739. doi: 10.1111/jam.14158.
[28] Alotaibi B, El-Masry TA, Elekhnawy E, et al. Aqueous core epigallocatechin gallate PLGA nanocapsules: characterization, antibacterial activity against uropathogens, and *in vivo* reno-protective effect in cisplatin induced nephrotoxicity. Drug Deliv. 2022;29(1):1848–1862. doi: 10.1080/10717544.2022.2083725.
[29] Attallah NG, Al-Fakhrany OM, Elekhnawy E, et al. Anti-biofilm and antibacterial activities of *Cycas media* R. Br secondary metabolites: *in silico*, *in vitro*, and *in vivo* approaches. Antibiotics. 2022;11(8):993.
[30] Batiha GES, Al-Gareeb AI, Elekhnawy E, et al. Potential role of lipoxin in the management of COVID-19: a narrative review. Inflammopharmacology. 2022;30(6):1993–2001. doi: 10.1007/s10787-022-01070-3.
[31] Al-Kuraishy HM, Al-Gareeb AI, Albogami SM, et al. Potential therapeutic benefits of metformin alone and in combination with sitagliptin in the management of type 2 diabetes patients with COVID-19. Pharmaceuticals. 2022;15(11):1361.

[32] Shiau AK, Barstad D, Loria PM, et al. The structural basis of estrogen receptor/coactivator recognition and the antagonism of this interaction by tamoxifen. Cell. 1998;95(7):927–937.
[33] Dawicki-McKenna JM, Langelier M-F, DeNizio JE, et al. PARP-1 activation requires local unfolding of an autoinhibitory domain. Mol Cell. 2015;60(5):755–768. doi: 10.1016/j.molcel.2015.10.013.
[34] Morris GM, Goodsell DS, Halliday RS, et al. Automated docking using a Lamarckian genetic algorithm and an empirical binding free energy function. J Comput Chem. 1998;19(14):1639–1662.
[35] Ali A, Said D, Khayyat M, et al. Improving the efficiency of the organic solar cell (CuPc/C60) via PEDOT: PSS as a photoconductor layer doped by silver nanoparticles. Results Phys. 2020;16:102819.
[36] Sachdev S, Ansari SA, Ansari MI, et al. Abiotic stress and reactive oxygen species: generation, signaling, and defense mechanisms. Antioxidants. 2021;10(2):277.
[37] Hasanuzzaman M, Bhuyan MB, Zulfiqar F, et al. Reactive oxygen species and antioxidant defense in plants under abiotic stress: revisiting the crucial role of a universal defense regulator. Antioxidants. 2020;9(8):681.
[38] Devireddy AR, Zandalinas SI, Fichman Y, et al. Integration of reactive oxygen species and hormone signaling during abiotic stress. Plant J. 2021;105(2):459–476. doi: 10.1111/tpj.15010.
[39] Kumar H, Bhardwaj K, Nepovimova E, et al. Antioxidant functionalized nanoparticles: a combat against oxidative stress. Nanomaterials. 2020;10(7):1334.
[40] Sedky NK, Fawzy IM, Hassan A, et al. Innovative microwave-assisted biosynthesis of copper oxide nanoparticles loaded with platinum (II) based complex for halting colon cancer: cellular, molecular, and computational investigations. RSC Adv. 2024;14(6):4005–4024. doi: 10.1039/d3ra08779d.
[41] Hublikar LV, Ganachari SV, Patil VB, et al. Anticancer potential of biologically synthesized silver nanoparticles using *Lantana camara* leaf extract. Prog Biomater. 2023;12(2):155–169. doi: 10.1007/s40204-023-00219-9.
[42] Kapoor G, Saigal S, Elongavan A. Action and resistance mechanisms of antibiotics: a guide for clinicians. J Anaesthesiol Clin Pharmacol. 2017;33(3):300–305. doi: 10.4103/joacp.JOACP_349_15.
[43] Al-Kuraishy HM, Al-Gareeb AI, Elekhnawy E, et al. Nitazoxanide and COVID-19: a review. Mol Biol Rep. 2022;49(11):11169–11176. doi: 10.1007/s11033-022-07822-2.
[44] El-Zamkan MA, Mohamed HM. Antimicrobial resistance, virulence genes and biofilm formation in *Enterococcus* species isolated from milk of sheep and goat with subclinical mastitis. PLOS One. 2021;16(11):e0259584. doi: 10.1371/journal.pone.0259584.
[45] Tuon FF, Dantas LR, Suss PH, et al. Pathogenesis of the *Pseudomonas aeruginosa* biofilm: a review. Pathogens. 2022;11(3):300. doi: 10.3390/pathogens11030300.
[46] Mohanta YK, Biswas K, Jena SK, et al. Anti-biofilm and antibacterial activities of silver nanoparticles synthesized by the reducing activity of phytoconstituents present in the Indian medicinal plants. Front Microbiol. 2020;11:1143. doi: 10.3389/fmicb.2020.01784.
[47] Pick A, Müller H, Mayer R, et al. Structure–activity relationships of flavonoids as inhibitors of breast cancer resistance protein (BCRP). Bioorg Med Chem. 2011;19(6):2090–2102.
[48] Katayama K, Masuyama K, Yoshioka S, et al. Flavonoids inhibit breast cancer resistance protein-mediated drug resistance: transporter specificity and structure–activity relationship. Cancer Chemother Pharmacol. 2007;60(6):789–797. doi: 10.1007/s00280-007-0426-7.
[49] Wang X, Yang Y, An Y, et al. The mechanism of anticancer action and potential clinical use of kaempferol in the treatment of breast cancer. Biomed Pharmacother. 2019;117:109086. doi: 10.1016/j.biopha.2019.109086.
[50] Luo H, Rankin GO, Li Z, et al. Kaempferol induces apoptosis in ovarian cancer cells through activating p53 in the intrinsic pathway. Food Chem. 2011;128(2):513–519. doi: 10.1016/j.foodchem.2011.03.073.